Electronic Supplementary Material (ESI) for Energy & Environmental Science.

Supplementary information

Ferroelectrically augmented contact electrification enables efficient acoustic energy transfer through liquid and solid media

Hyun Soo Kim [a, b], Sunghoon Hur [a], Dong-Gyu Lee [a, c], Joon-Chul Shin [a], Huimin Qiao [d], Seunguk Mun [d], Hoontaek Lee [e], Wonkyu Moon [e], Yunseok Kim [d], Jeong Min Baik [d], Chong-Yun Kang [a, f], Jong Hoon Jung [b, *], and Hyun-Cheol Song [a, d, g, *]

[a] Electronic Materials Research Center, Korea Institute of Science and Technology (KIST), Seoul 02792, Republic of Korea

[b] Department of Physics, Inha University, Incheon 22212, Republic of Korea

[c] Department of Materials Science and Engineering, Korea University, Seoul 02841, Republic of Korea

[d] School of Advanced Materials Science and Engineering, Sungkyunkwan University (SKKU), Suwon 16419, Republic of Korea

[e] Department of Mechanical Engineering, Pohang University of Science and Technology, Pohang 37673, Republic of Korea

[f] KU-KIST Graduate School of Converging Science and Technology, Korea University, Seoul 02841, Republic of Korea

[g] KHU-KIST Department of Converging Science and Technology, Kyung Hee University, Yongin 17104, Republic of Korea

*Corresponding Authors: jhjung@inha.ac.kr and hcsong@kist.re.kr

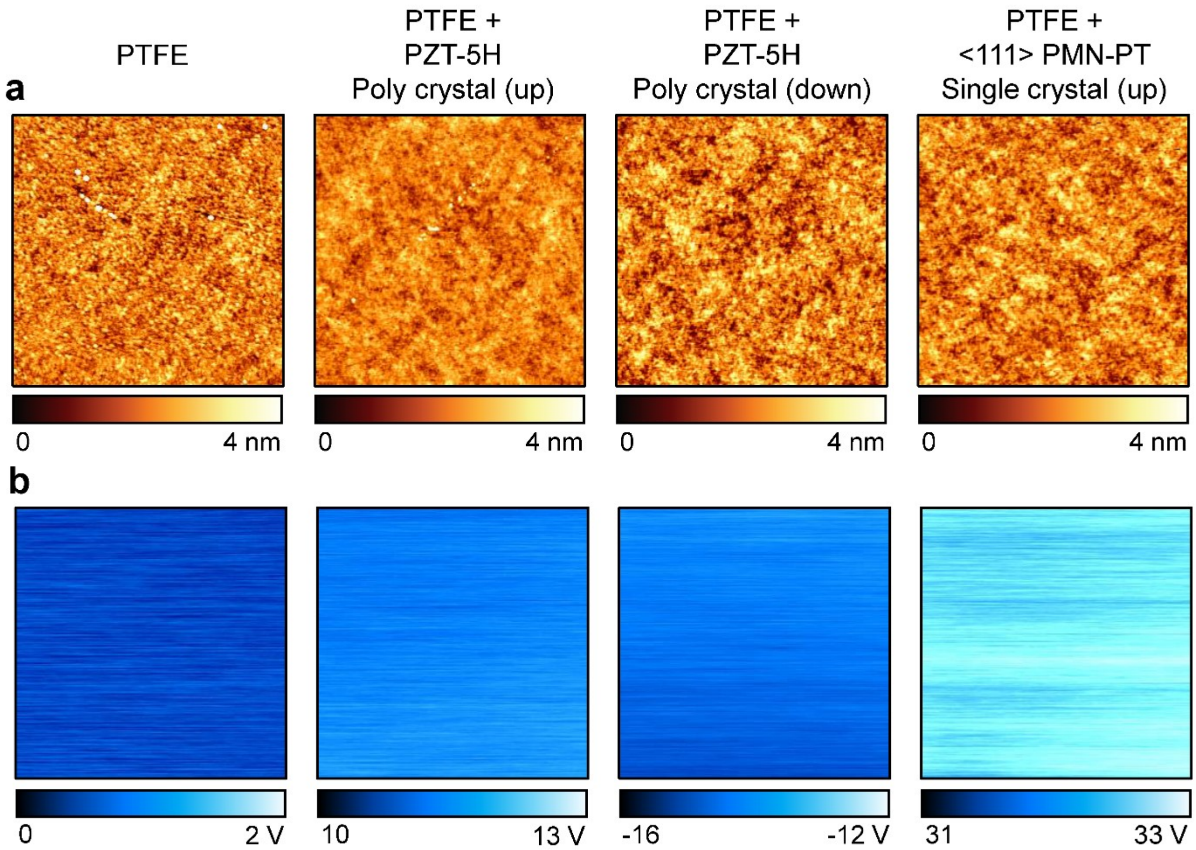

Fig. S1 (a) Topography and (b) KPFM images. The roughness (Rq) of each topography image in Fig. (a) is 0.74, 0.55, 0.62, and 0.61nm, respectively. The KPFM images present modulated CPD of PTFE surface by ferroelectric ceramics (area of 3×3 μm^2).

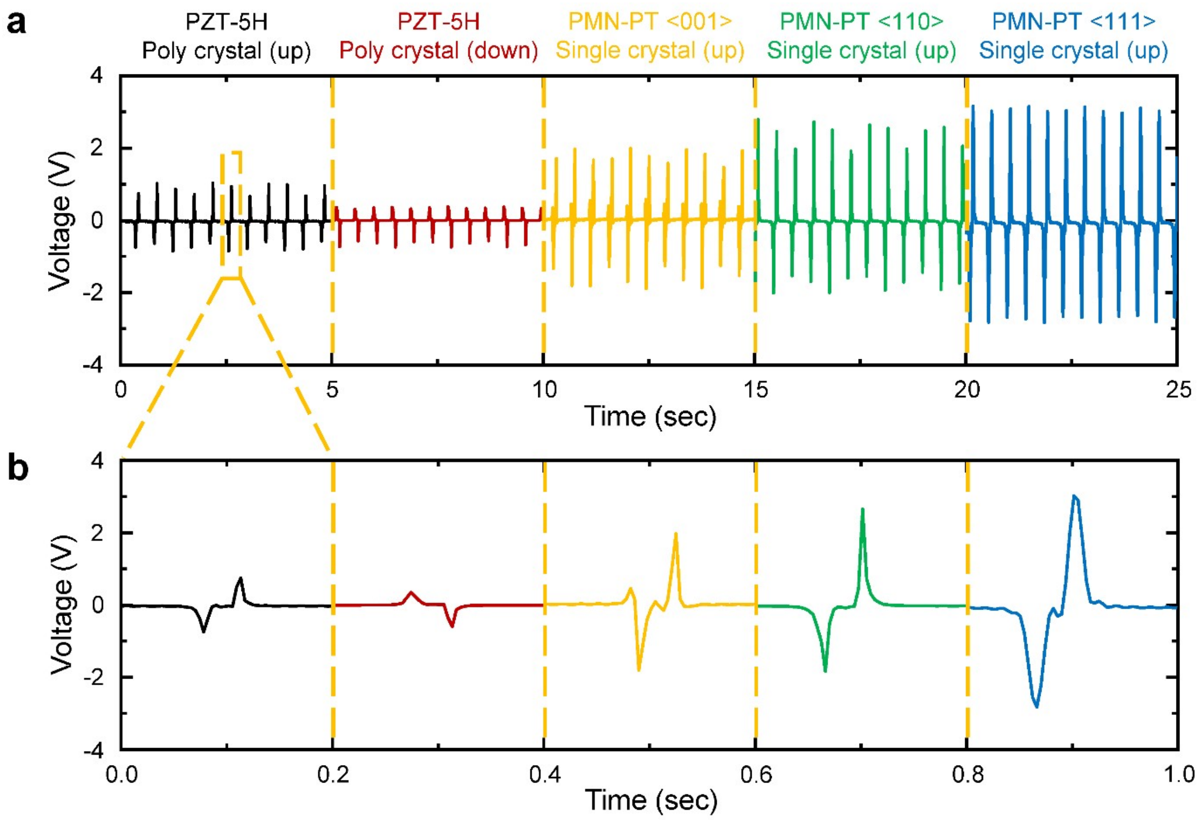

Fig. S2 Performance of ferroelectric ceramic-based devices without PTFE. (a) Open-circuit voltage and (b) Magnified view during one contact-separation cycle.

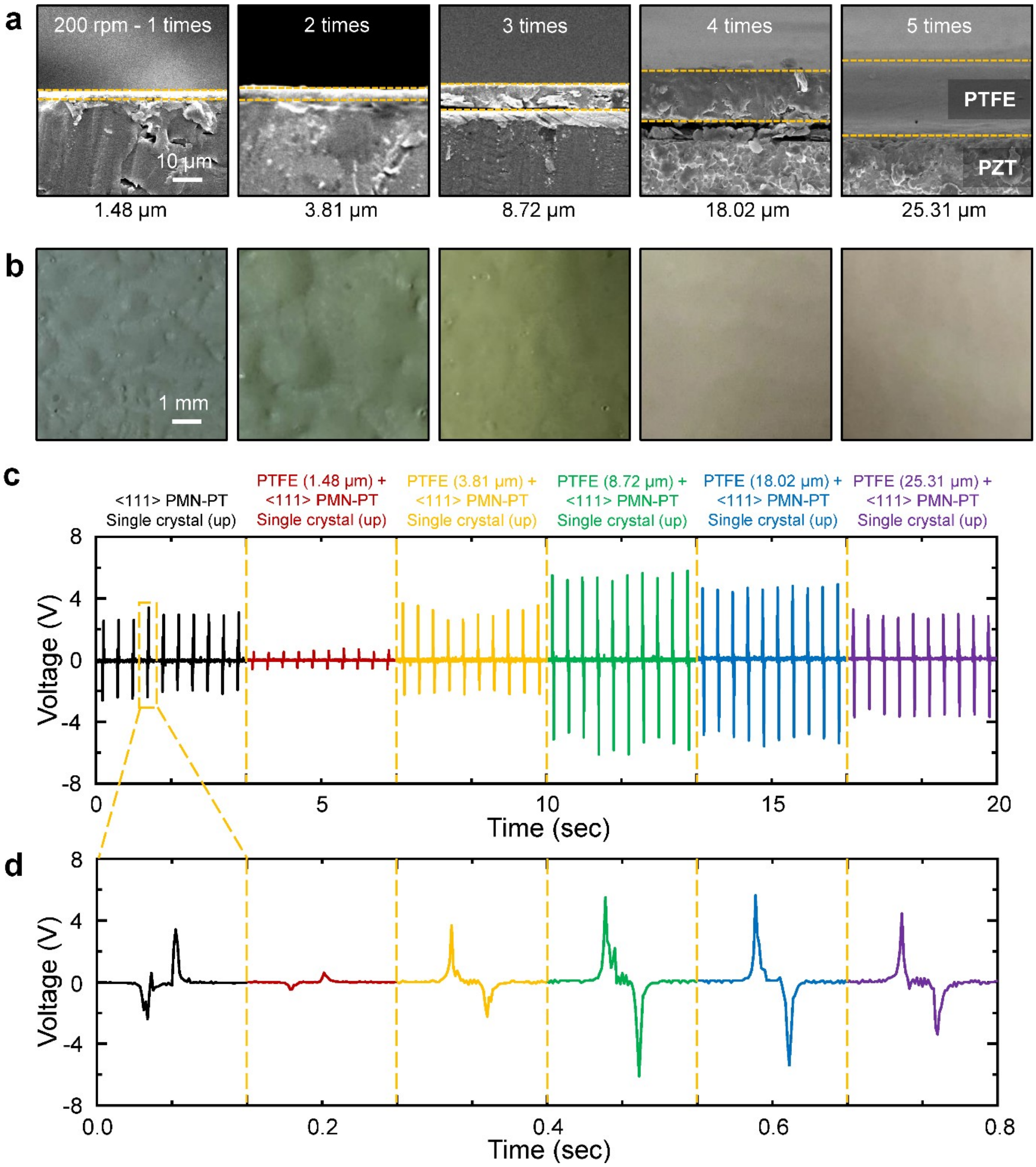

Fig. S3 PTFE thickness optimization. (a) Cross-sectional SEM and (b) Top-view optical images of PTFE on ferroelectric ceramics. (c) PTFE thickness-dependent open-circuit voltage. (d) Magnified view during one contact-separation cycle.

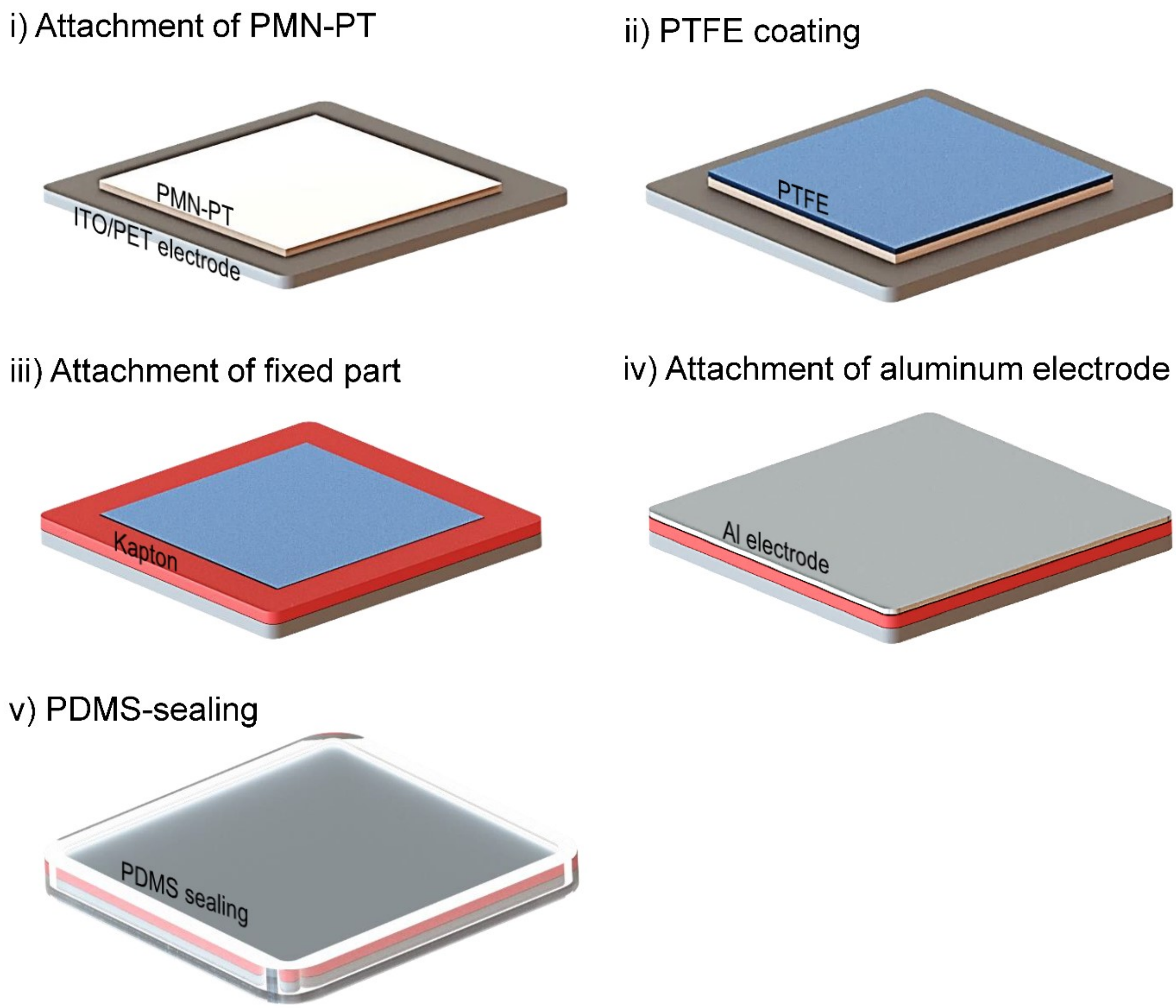

Fig. S4 Fabrication process of the triboelectric AET receiver.

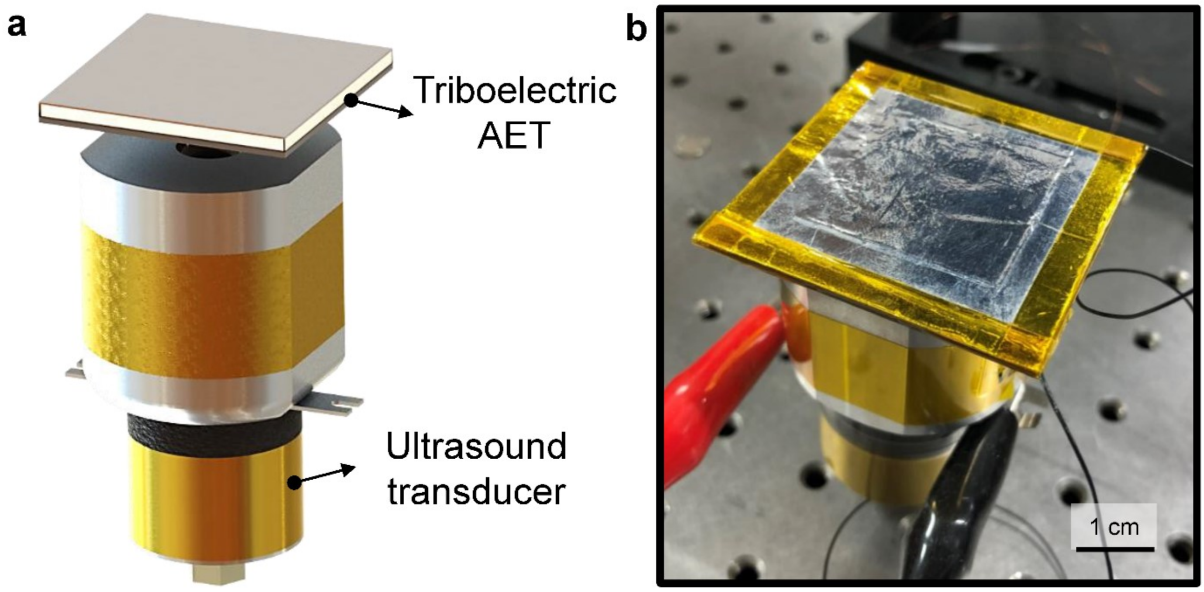

Fig. S5 Triboelectric AET device with an ultrasound transducer. (a) Schematic illustration and (b) Optical image.

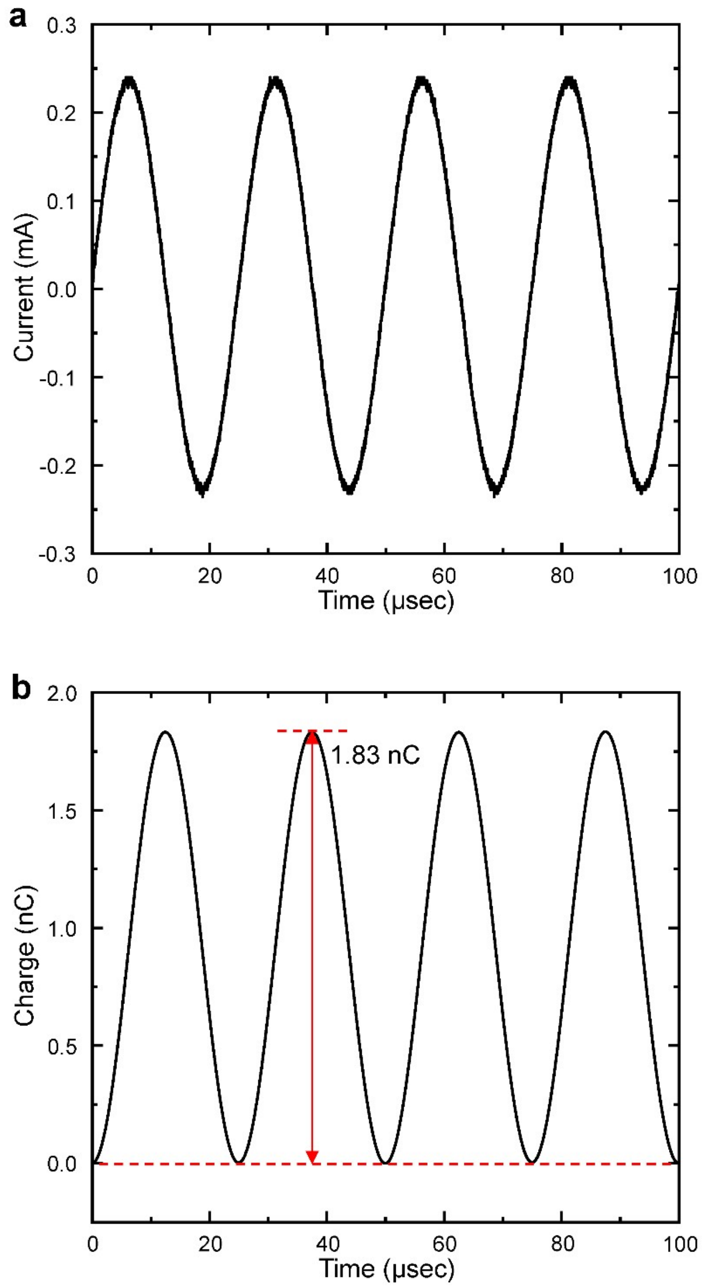

Fig. S6 Triboelectric AET receiver performance. (a) Short-circuit current and (b) Charge.

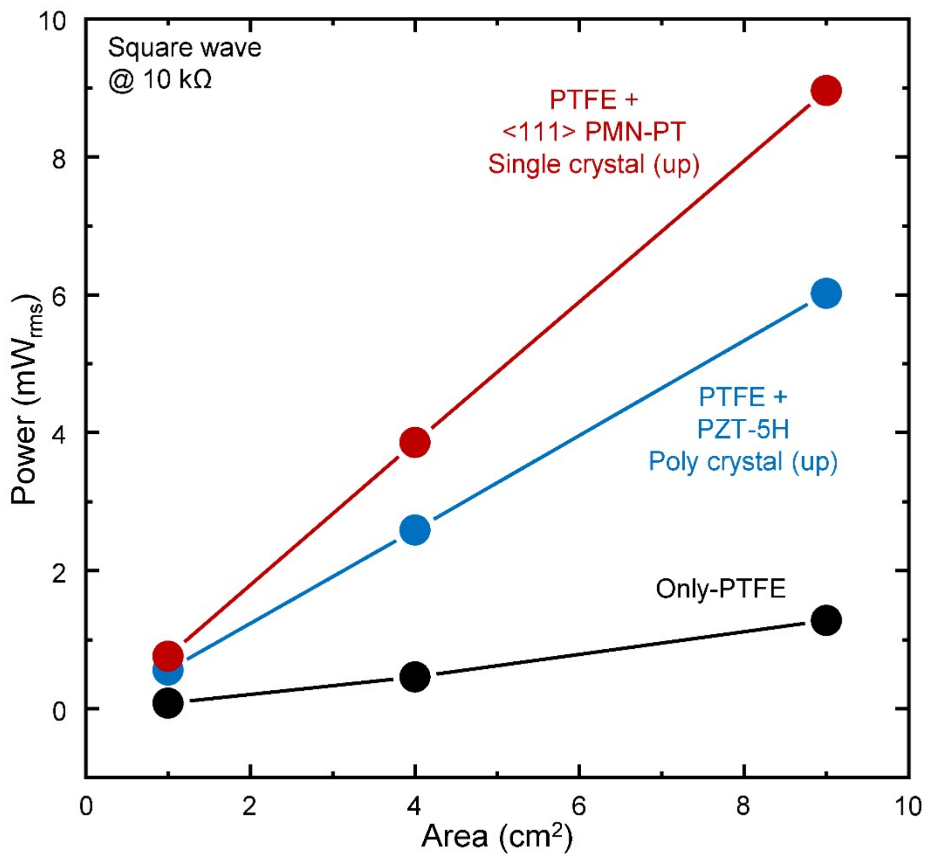

Fig. S7 Area-dependent output performance of AET.

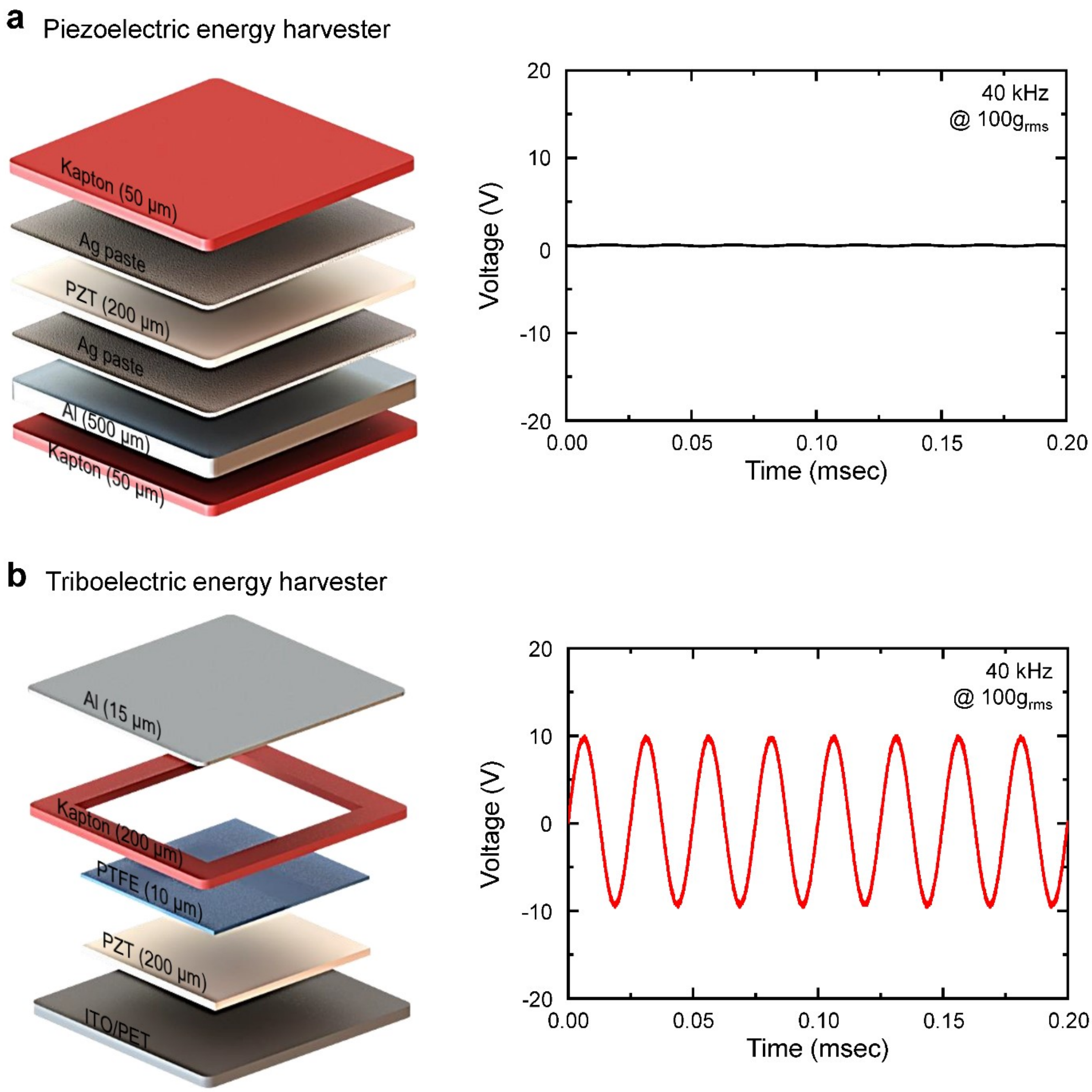

Fig. S8 Compared output performance. Schematic diagram and output voltage for (a) piezoelectric-based and (b) triboelectric-based AETs.

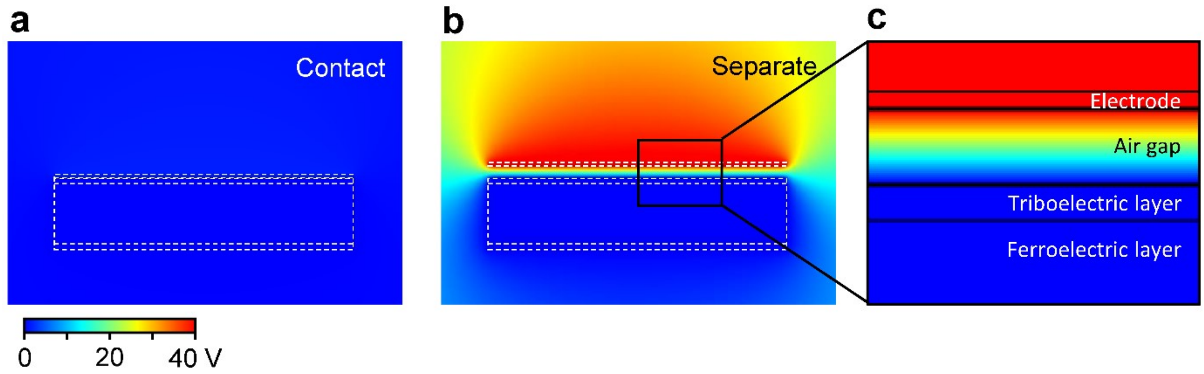

Fig. S9 Finite element analysis simulated electrical potential image of the ferroelectrically boosted triboelectric energy receiver under 40 kHz ultrasound wave condition. (a) Contact and (b) Separation states. (c) Magnified electrical potential distribution near the air gap.

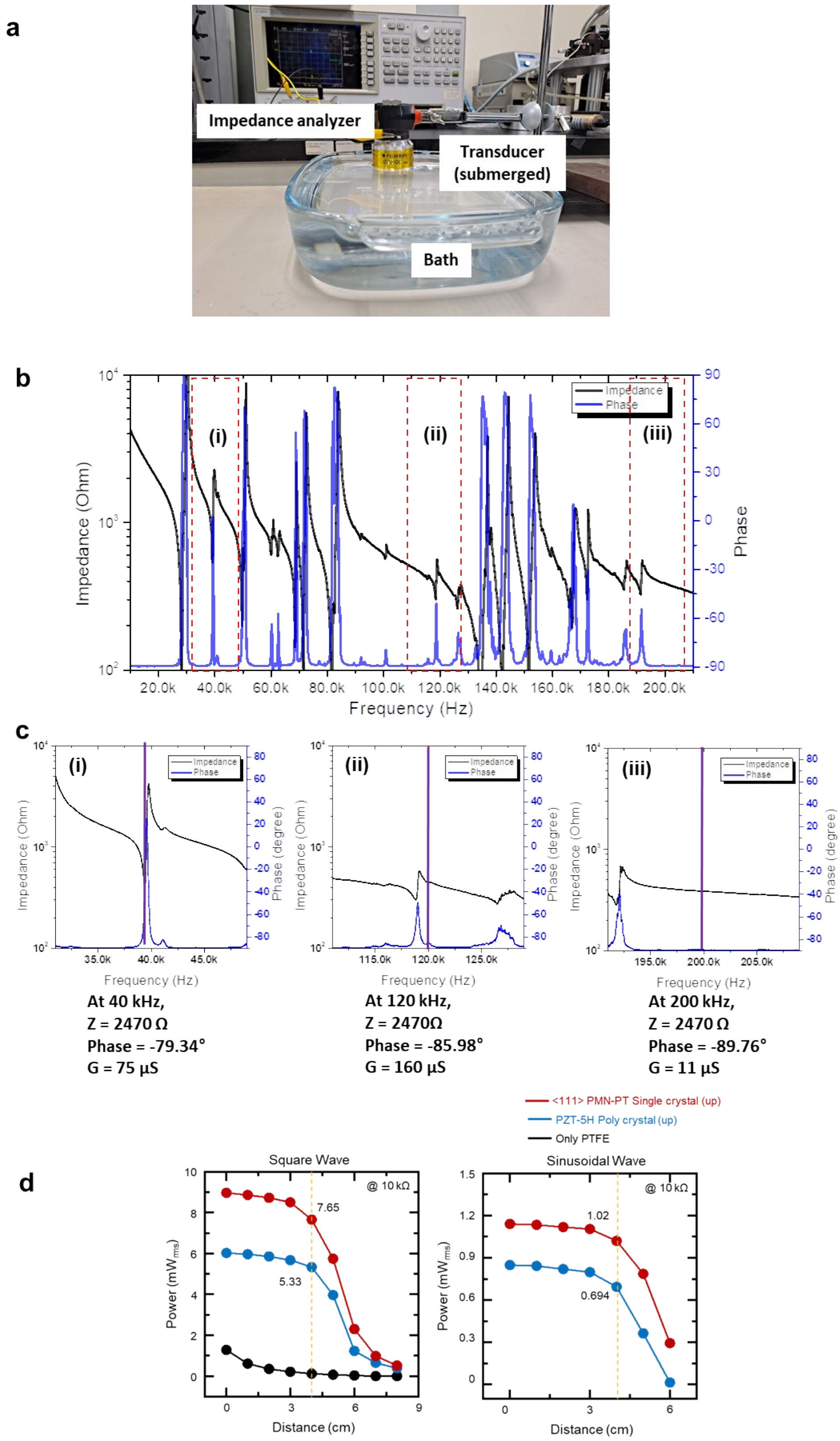

Fig. S10. (a) Experimental setup for impedance analysis (b) Graph of impedance and phase from 10 kHz to 210 kHz. (c) Expanded view of impedance analysis in 40 kHz, 120 kHz, and 200 kHz region for acquiring accurate conductance values. (d) Power generation on the receiver under square and sinusoidal voltage input into the transducer.

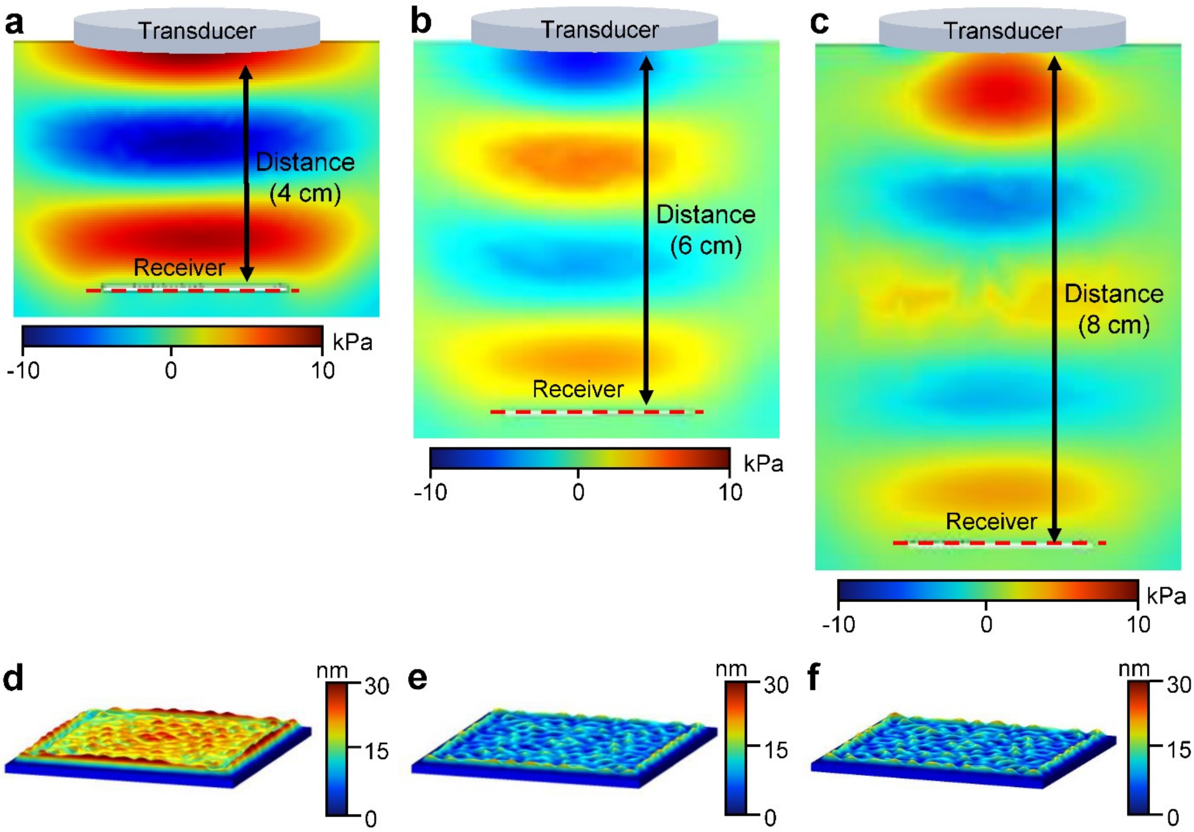

Fig. S11 COMSOL simulation of distance-dependent acoustic pressure in water and displacement of the flexible electrode. Simulated acoustic pressure distribution and displacement for the distance of (a, d) 4 cm, (b, e) 6 cm, and (c, f) 8 cm from ultrasound transducer to receiver.

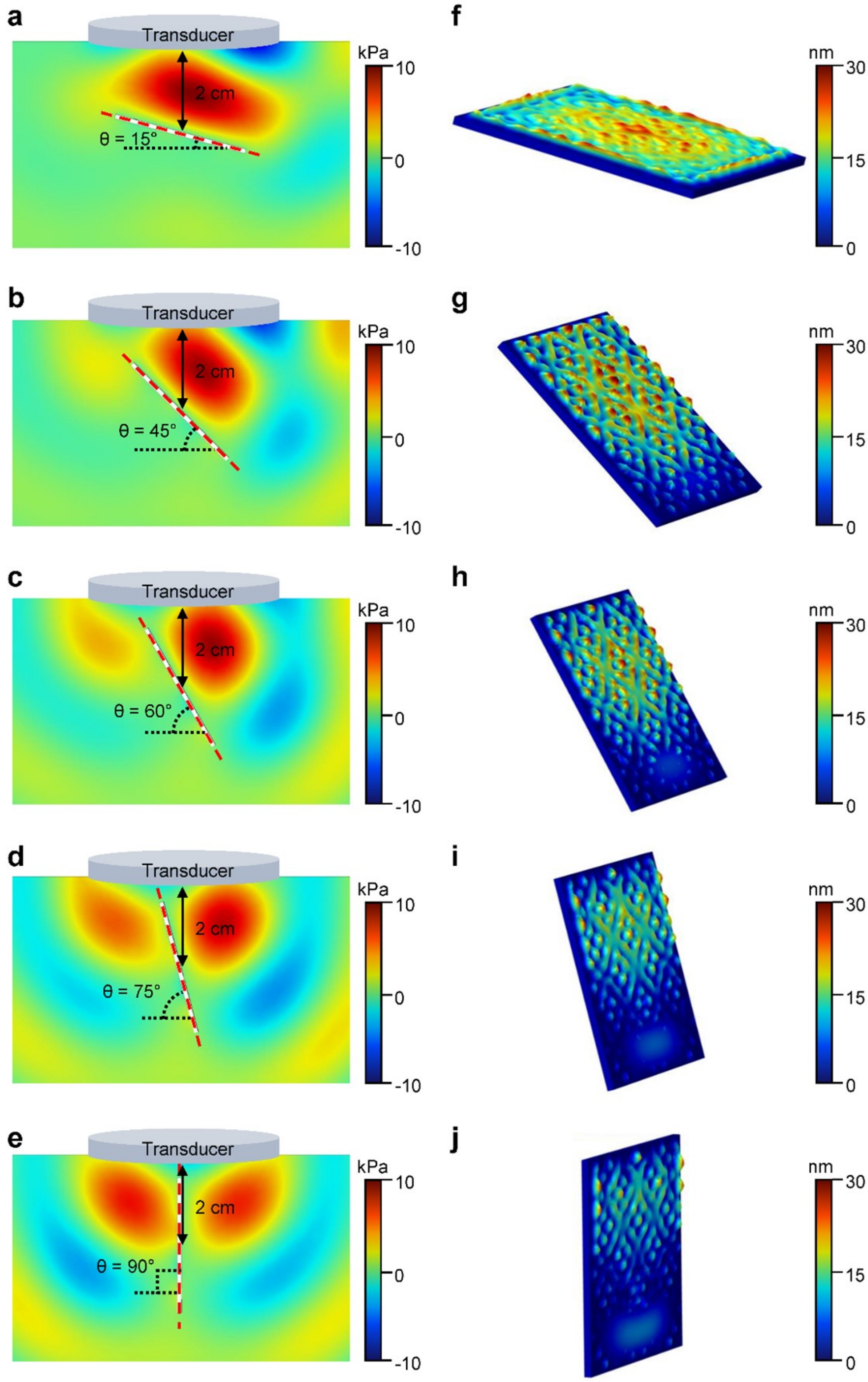

Fig. S12 COMSOL simulation of tilting angle-dependent acoustic pressure in water and displacement of the flexible electrode. Simulated acoustic pressure distribution and displacement for tilting angle of (a, f) 15 degree, (b, g) 45 degree, (c, h) 60 degree, (d, i) 75 degree, and (e, j) 90 degree from ultrasound transducer to receiver.

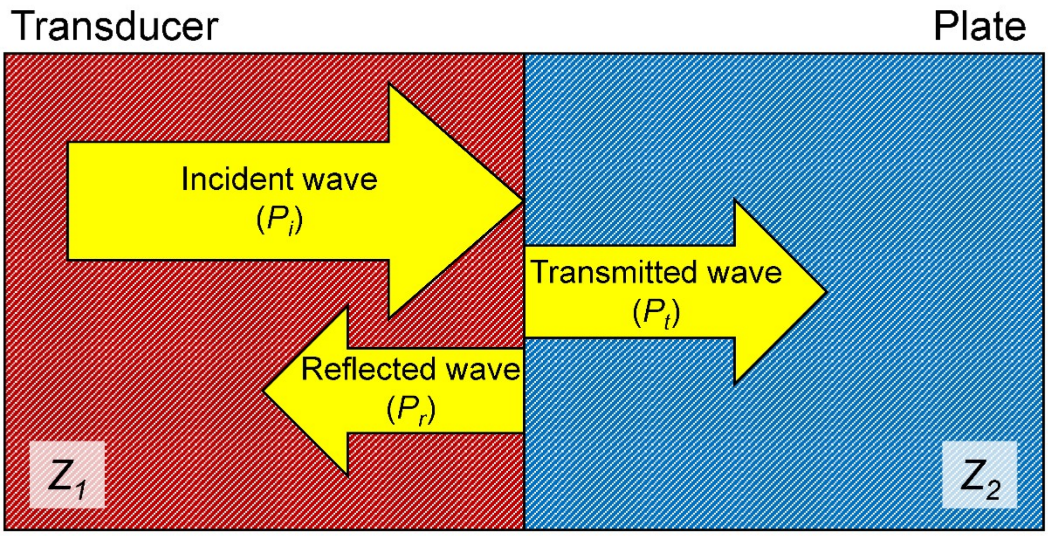

$$Z = \frac{P}{vS}$$

$$I = \frac{P^2}{\rho C}$$

Z : Acoustic impedance
P : Sound pressure
v : Particle velocity
S : Area
ρ : Density
C : Sound speed

Pressure reflection coefficient : $R = \frac{P_r}{P_i} = \frac{Z_2 - Z_1}{Z_2 + Z_1}$

Pressure transmission coefficient : $T = 1 - R = \frac{2Z_1}{Z_2 + Z_1}$

Intensity reflection coefficient : $R = \frac{I_r}{I_i} = \frac{(Z_2 - Z_1)^2}{(Z_2 + Z_1)^2}$

Intensity transmission coefficient : $T = 1 - R = \frac{4Z_2Z_1}{(Z_2 + Z_1)^2}$

Fig. S13 Schematic illustration of the acoustic reflection and transmission coefficient calculation.

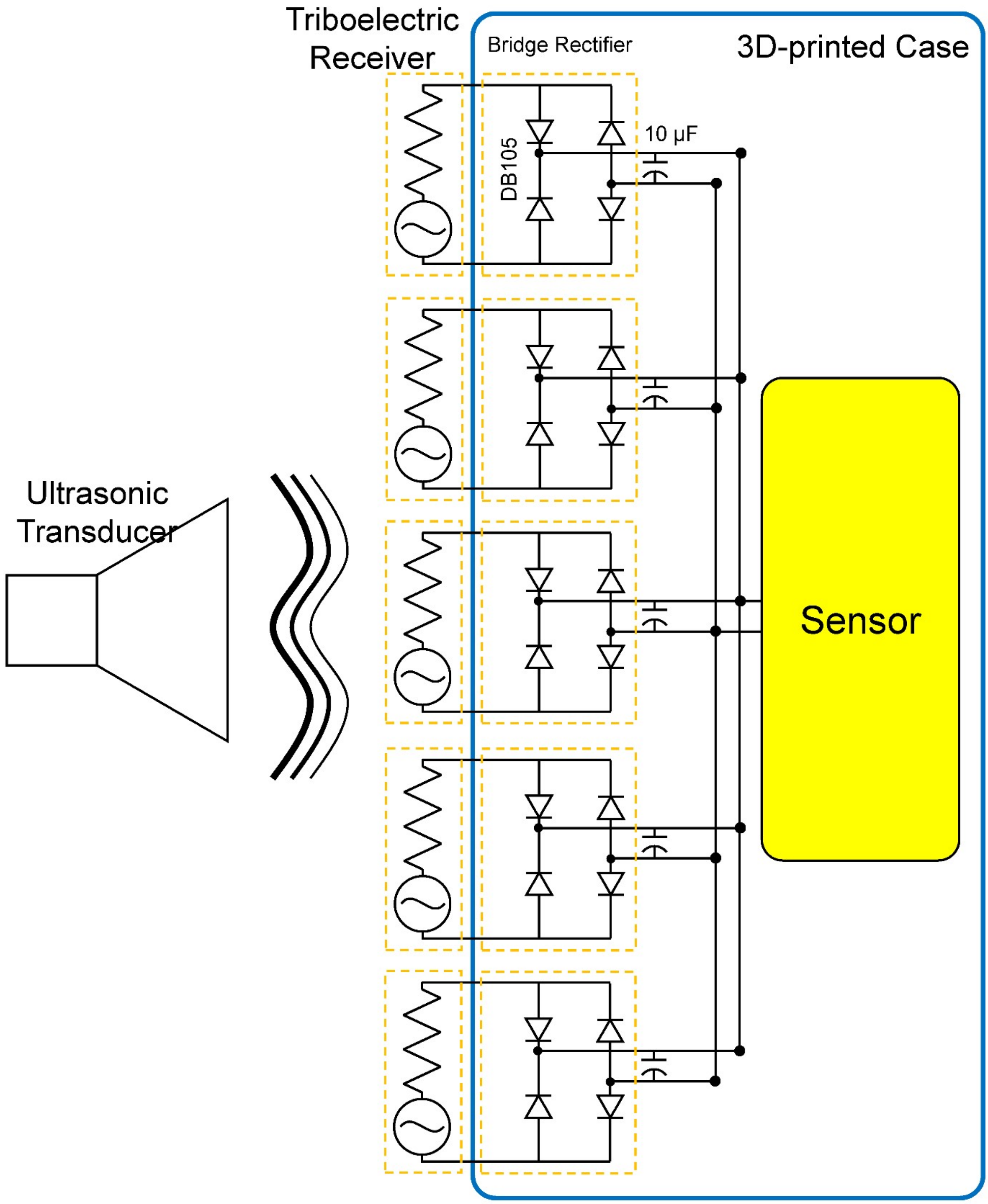

Fig. S14 A schematic circuit diagram for the continuous operating wireless sensor.

Table S1 Comparison of the relevant previous reports and this work.

Reference	Year	Working principle	Ultrasound frequency (kHz)	Distance (mm)	Power density (mW/cm^2)	Features
P. Shih and W. Shih [1]	2010	Piezoelectric	35	15	2.6×10^{-5}	Tested in fatty/muscular tissue
Fowler, A.G, et al.[2]	2014	Piezoelectric	25	50	7.5×10^{-4}	MEMS device
Shi. Q.F., et al.[3]	2016	Piezoelectric	240	10	3.75 × 10-3	MEMS device
Sun, Y.Q., et al.[4]	2018	Piezoelectric	600	40	0.8	Used a concave shape receiver
Jiang, L.M., et al.[[5]	2019	Piezoelectric	350	14	4.1×10^{-3}	Adopt 1-3 composite arrays
Jiang, L.M., et al.[6]	2021	Piezoelectric	1000 ~ 3300	12	21	Received a high-intensity focused acoustic wave, resulting in power enhancement
Hinchet, R., et al.[7]	2019	Triboelectric	20	5	5.2×10^{-1}	First conceptual triboelectric ultrasound receiver
Chen, C., et al.[8]	2020	Triboelectric	100	30	1.2×10^{-6}	MEMS device
Lee, K.H, et al.[9]	2020	Triboelectric	20	2	4.3×10^{-3}	Adopt MXene hydrogel
This work		**Triboelectric**	**10 ~ 60**	**30 ~ 60**	**9 ~ 2.2**	**Incorporate a square wave and ferroelectrics, resulting in effective/robust power transmission**

Table S2 Acoustic reflection and transmission coefficient.

Material	Acoustic impedance (MRayls)	Pressure reflection coefficient (%)	Pressure transmission coefficient (%)	Intensity reflection coefficient (%)	Intensity transmission coefficient (%)
Conductive metal	46.4	7.04	92.96	0.50	99.50
Acryl plate	3.26	85.03	14.97	72.30	27.70
Wood	1.57 ~ 2.9	56.57~ 92.50	7.50~13.43	74.95~85.56	14.44~ 25.05

Video. S1 The fluctuation of flexible aluminum electrode observed using the laser vibrometer.

Video. S2 Charging capacitor by the triboelectric acoustic energy transmission (AET) receiver at 100 g_{rms} acceleration and 1 cm depth.

Video. S3 Powering 200 light-emitting diodes (LEDs) by the triboelectric acoustic energy transmission (AET) receiver at 100 g_{rms} acceleration and 6 cm depth.

Video. S4 Operation of IoT sensor by the triboelectric acoustic energy transmission (AET) receiver at 100 g_{rms} acceleration and 6 cm depth.

References

1. Shih, P.J. and W.P. Shih, *Design, Fabrication, and Application of Bio-Implantable Acoustic Power Transmission.* Journal of Microelectromechanical Systems, 2010. **19**(3): p. 494-502.
2. Fowler, A.G., S.O.R. Moheimani, and S. Behrens, *An Omnidirectional MEMS Ultrasonic Energy Harvester for Implanted Devices.* Journal of Microelectromechanical Systems, 2014. **23**(6): p. 1454-1462.
3. Shi, Q.F., T. Wang, and C. Lee, *MEMS Based Broadband Piezoelectric Ultrasonic Energy Harvester (PUEH) for Enabling Self-Powered Implantable Biomedical Devices.* Scientific Reports, 2016. **6**.
4. Sun, Y.Q., et al., *A wideband ultrasonic energy harvester using 1-3 piezoelectric composites with non-uniform thickness.* Applied Physics Letters, 2018. **112**(4).
5. Jiang, L.M., et al., *Flexible piezoelectric ultrasonic energy harvester array for bio-implantable wireless generator.* Nano Energy, 2019. **56**: p. 216-224.
6. Jiang, L.M., et al., *Photoacoustic and piezo-ultrasound hybrid-induced energy transfer for 3D twining wireless multifunctional implants.* Energy & Environmental Science, 2021. **14**(3): p. 1490-1505.
7. Hinchet, R., et al., *Transcutaneous ultrasound energy harvesting using capacitive triboelectric technology.* Science, 2019. **365**(6452): p. 491.
8. Chen, C., et al., *Micro triboelectric ultrasonic device for acoustic energy transfer and signal communication.* Nature Communications, 2020. **11**(1).
9. Lee, K.H., et al., *Ultrasound-Driven Two-Dimensional $Ti_3C_2T_x$ MXene Hydrogel Generator.* Acs Nano, 2020. **14**(3): p. 3199-3207.